

Near-Infrared Afterglow Luminescence of Chlorin Nanoparticles for Ultrasensitive *In Vivo* Imaging

Wan Chen, Yuan Zhang, Qing Li,* Yue Jiang, Hui Zhou, Yinghua Liu, Qingqing Miao,* and Mingyuan Gao*



Cite This: *J. Am. Chem. Soc.* 2022, 144, 6719–6726



Read Online

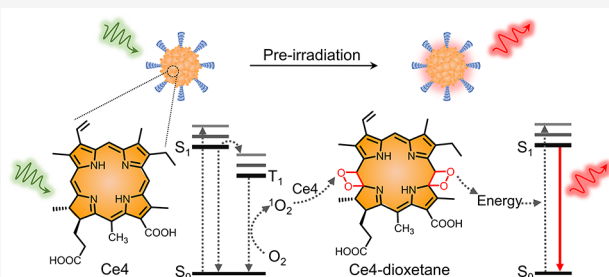
ACCESS |

Metrics & More

Article Recommendations

Supporting Information

ABSTRACT: Afterglow imaging holds great potential for ultrasensitive biomedical imaging. As it detects photons after the cessation of real-time light excitation, autofluorescence can therefore be effectively eliminated. However, afterglow imaging is still in its infant stage due to the lack of afterglow agents with satisfactory lifetime, biocompatibility, and high luminescence brightness, particularly afterglow in the near-infrared region for *in vivo* applications. To address these issues, this study for the first time reports chlorin nanoparticles (Ch-NPs) emitting afterglow luminescence peaking at 680 nm with a half-life of up to 1.5 h, which is almost 1 order of magnitude longer than those of other reported organic afterglow probes. In-depth experimental and theoretical studies revealed that the brightness of the afterglow luminescence is strongly correlated with the singlet oxygen ($^1\text{O}_2$) capacity and the oxidizability of the chlorins. Benefiting from the ultralong half-life and the minimized imaging background, small metastatic tumor foci of 3 mm^3 were successfully resected under the guidance of the afterglow luminescence generated upon a single shot of activation prior to the injection, which was impossible for conventional near-infrared fluorescence imaging due to tissue autofluorescence.



INTRODUCTION

Optical imaging that capitalizes on the detection of photons to decipher molecular and biological processes offers powerful tools for biology and medicine.^{1–3} However, as a commonly used optical imaging technique, fluorescence imaging requires real-time light excitation that induces tissue autofluorescence and consequently results in a compromised signal-to-noise ratio (SNR) and a reduced tissue detection depth, unfavorable for imaging sensitivity and specificity.^{4,5} Hence, self-luminescence imaging approaches including chemiluminescence, bioluminescence, and afterglow luminescence that require no real-time light excitation have attracted increasing enthusiasm in recent years to circumvent tissue autofluorescence.^{6–11} However, chemiluminescence and bioluminescence imaging rely on reactive species- and enzyme-initiated redox reactions to trigger luminescence, respectively.^{12,13} Their imaging signals are easily perturbed by internal stimuli such as the enzymatic or redox microenvironment and the availability of the substrate.^{14,15} In comparison with fluorescence, the afterglow luminescence only requires preillumination of afterglow agents; in comparison with chemiluminescence and bioluminescence, the afterglow luminescence requires no particular chemical mediator or exogenous enzyme, which highlights the advantages of the latter approach for biomedical applications.^{16,17}

Nevertheless, afterglow luminescence imaging does need afterglow luminescent agents comprising inorganic or organic active materials that have been used for tumor imaging,^{18–25} lymph node mapping,^{22,26} imaging of drug-induced hepatotoxicity,²⁶ monitoring of drug release,²⁷ specific detection of cancer exosomes,²⁸ imaging of blood vessels,²⁹ predicting anticancer efficiency,³⁰ and imaging-guided therapy.^{31–33} In comparison with the inorganic luminescence materials, better biosafety profile and easier afterglow luminescence tunability are expected from the organic counterparts.^{34,35} To date, there are only a few organic afterglow systems reported based on either semiconducting polymers or small molecular systems comprising multiple ingredients.^{23,26,30,36} However, due to the short wavelength and the relatively low intensity of the afterglow luminescence, efforts including implemental amplification, cascade red-shifted strategies, and optimization of the molecular structure through complex organic synthesis are being made.^{20,22} Unfortunately, the afterglow agents reported so far exhibit a short half-life of several minutes, and therefore

Received: September 25, 2021

Published: April 5, 2022



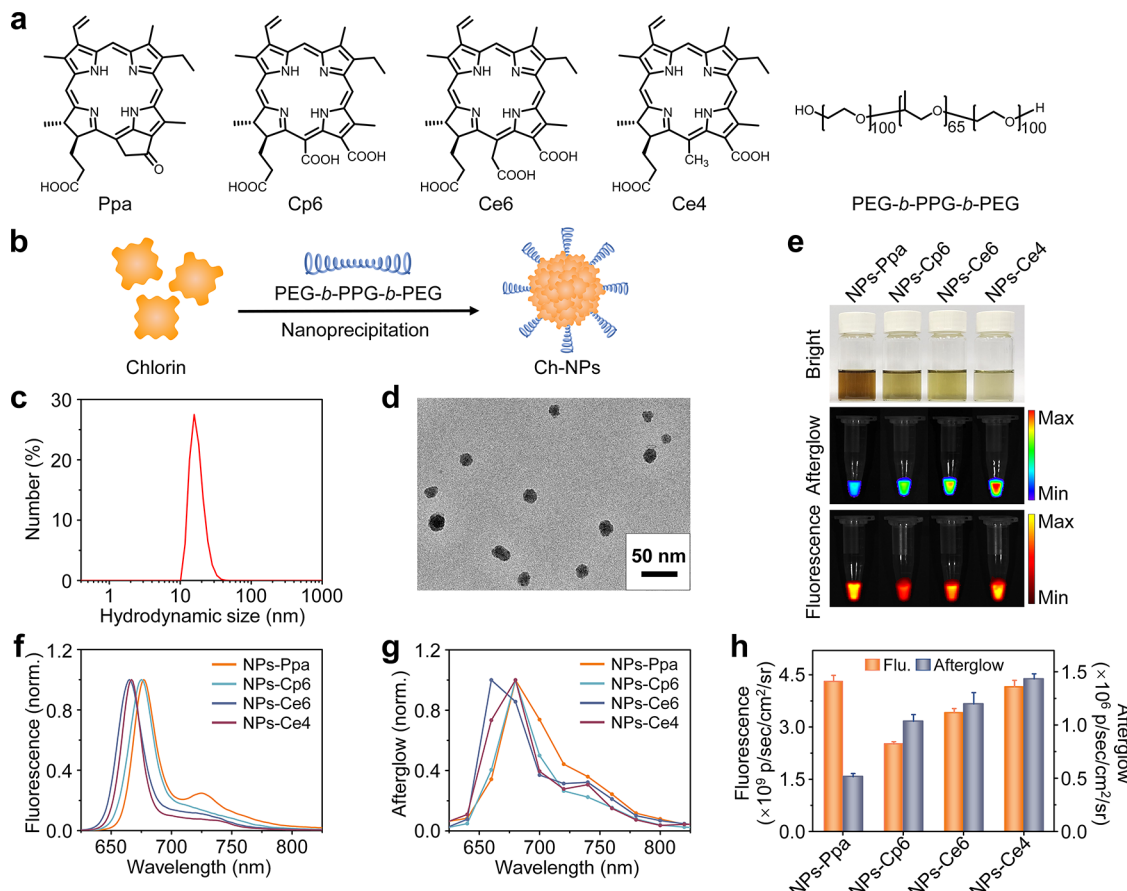


Figure 1. Structural characterization and afterglow performance of Ch-NPs. (a) Chemical structures of chlorins and PEG-*b*-PPG-*b*-PEG. (b) Schematic illustration of the preparation of Ch-NPs. (c) Hydrodynamic size distribution profile of NPs-Ce4 in 1× PBS buffer. (d) Representative TEM image of NPs-Ce4. (e) Bright-field (upper panel), afterglow (middle panel), and fluorescence (bottom panel) images of Ch-NPs of 50 μM with respect to chlorin molecules in 1× PBS buffer. The afterglow images were captured after the Ch-NPs were illuminated with a 1 cm (radius) 0.1 W/cm² light beam generated by a halogen lamp for 1 min. The fluorescence images were captured with excitation and emission at 430 and 680 nm, respectively, on an IVIS Spectrum imaging system. (f) Normalized fluorescence spectra of Ch-NPs in 1× PBS buffer under excitation at 400 nm. (g) Normalized afterglow luminescence spectra of Ch-NPs in 1× PBS buffer. (h) Structural dependency of afterglow and fluorescence, and the error bars represent the standard deviation ($n = 3$).

repeated *in situ* light irradiation is required to reactivate afterglow luminescence during the imaging process, which hampers its feasibility for long-term imaging.^{26,27,32} Thus, organic afterglow agents showing intrinsic near-infrared emission with a long lifetime are highly demanded not only for fundamental study but also for potential clinical applications.

In this study, we report the first series of chlorin-based afterglow agents showing an extraordinarily long lifetime for ultrasensitive imaging of tumors *in vivo*. Different from previous multicomponent afterglow systems, the current small molecular chlorin simultaneously acts as both an ${}^1\text{O}_2$ initiator and an afterglow producer that emits intrinsic near-infrared afterglow luminescence with a half-life of up to 1.5 h. To show the underlying mechanism, a series of chlorin derivatives were carefully selected to prepare chlorin nanoparticles (Ch-NPs) for comparing their afterglow luminescence. By combining the absorption spectroscopy, high-performance liquid chromatography (HPLC), and mass spectroscopy (MS) results with theoretical calculations, the unique afterglow behaviors of chlorin molecules were investigated. The application of Ch-NPs for imaging-guided resection of small metastatic tumor foci was further

demonstrated to show the advantage of afterglow luminescence over conventional fluorescence with respect to imaging sensitivity.

RESULTS AND DISCUSSION

Structural Dependency of Chlorin Derivatives for Afterglow Luminescence. Originally, we discovered that chlorin e6 (Ce6) was able to generate afterglow luminescence upon light irradiation. To show the underlying mechanism and optimize the afterglow performance, a series of chlorin derivatives including pyropheophorbide a (Ppa), chlorin p6 (Cp6), Ce6, and chlorin e4 (Ce4) were selected, as given in Figure 1a, to construct Ch-NPs for the mechanistic study of the afterglow luminescence. Among them, chlorin p6 was synthesized according to the route reported in the literature (Scheme S1),³⁷ and the MS analysis is given in Figure S1. Because all of these chlorins are hydrophobic, an amphiphilic triblock copolymer (PEG-*b*-PPG-*b*-PEG) was used as a surface capping agent to obtain aqueous-dispersible Ch-NPs as described in Figure 1b. Taking the particle formed by Ce4 (denoted as NPs-Ce4) as an example, the hydrodynamic size of NPs-Ce4 was 14.9 ± 1.2 nm (Figure 1c). Under transmission electron microscopy (TEM), they are quasi-

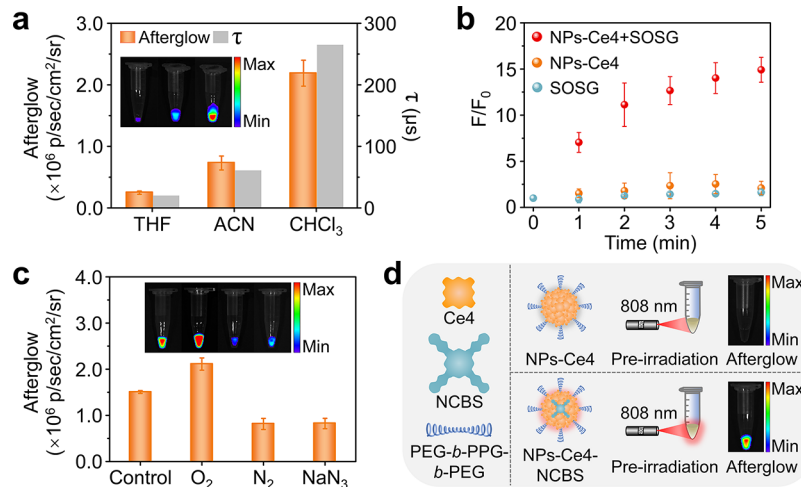


Figure 2. Elucidation of the role of $^1\text{O}_2$ in the afterglow of chlorins. (a) Afterglow intensity of Ce4 of $30 \mu\text{g}/\text{mL}$ in THF, ACN, and CHCl_3 recorded after illumination with a halogen lamp for 1 min together with the corresponding $^1\text{O}_2$ lifetimes borrowed from refs 38–40. (b) Temporal concentration of $^1\text{O}_2$ generated by NPs-Ce4 ($2 \mu\text{g}/\text{mL}$), represented by the fluorescence enhancement (F/F_0) of a singlet oxygen sensor SOSG ($1 \mu\text{M}$), as a function of the halogen lamp irradiation time. (c) Afterglow intensities of NPs-Ce4 ($30 \mu\text{g}/\text{mL}$) recorded before and after being purged with O_2 and N_2 , and introducing 50% w/w of NaN_3 into the aqueous system. (d) Schematic illustrations for generating the afterglow from NPs-Ce4 and NPs-Ce4-NCBS after irradiation with an 808 nm laser ($1 \text{W}/\text{cm}^2$) for 1 min.

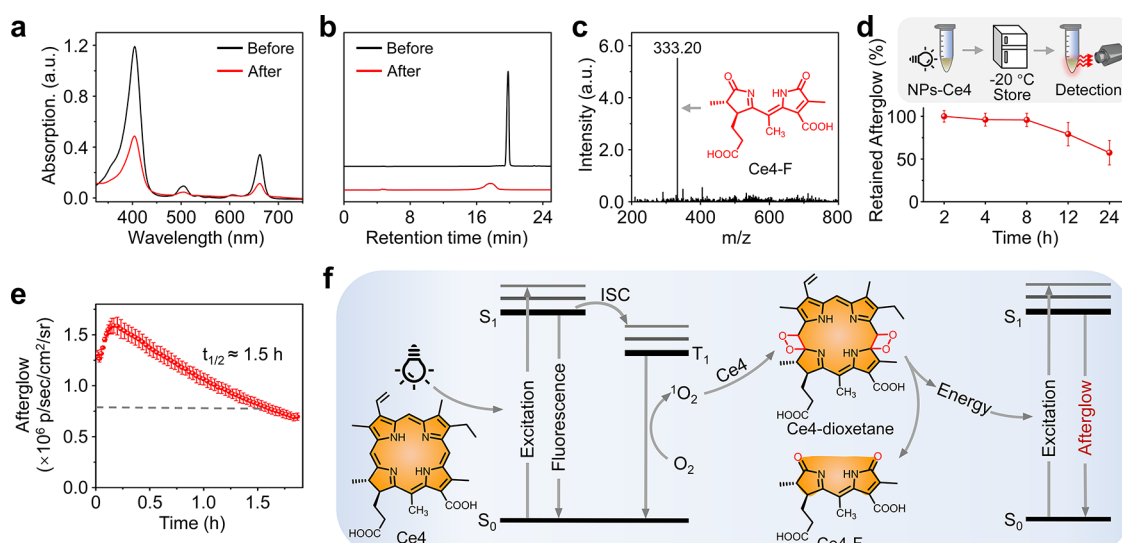


Figure 3. Mechanistic study of the afterglow of chlorins. (a) Ultraviolet-visible (UV-vis) absorption spectra of NPs-Ce4 ($5 \mu\text{g}/\text{mL}$) recorded before and after radiation with a halogen lamp for 30 min in $1\times$ PBS buffer. (b) HPLC traces detected according to the absorption at 280 nm before and after Ce4 was irradiated for 30 min in ACN. (c) Mass spectrum of the newly formed substance with a retention time of 17.6 min and the structure shown in the inset. (d) Schematic illustration for showing the effect of low-temperature storage time on the retention of afterglow luminescence of NPs-Ce4 ($30 \mu\text{g}/\text{mL}$). (e) Afterglow luminescence decay of NPs-Ce4 ($30 \mu\text{g}/\text{mL}$) recorded at 37°C . (f) Possible mechanism proposed for afterglow luminescence of Ce4 (S_0 , S_1 , T_1 , and ISC represent singlet ground state, first excited singlet state, first excited triplet state, and intersystem crossing, respectively). The embedded error bars represent standard deviation ($n = 3$).

spherical as given in Figure 1d. Other Ch-NPs exhibited very comparable hydrodynamic diameters (Figure S2). Moreover, the aqueous dispersions of the resulting Ch-NPs formed by different types of chlorins were very colloidally stable (Figure 1e), and no precipitates were observed in the PBS buffer for over a month.

The optical properties of these chlorins were then carefully compared. In tetrahydrofuran (THF) solution, they all showed sharp Soret bands at about 400 nm, according to the ultraviolet-visible (UV-vis) absorption spectra shown in Figure S3a. But Ppa presented a broadened Soret band after forming nanoparticles (Figure S3b), which may be attributed

to the impact of the substituents on the chlorin backbone on the stacking structure of chlorin molecules. Before collecting the afterglow signals, the light irradiation time was optimized (Figure S4), taking Ce4 as an example. As given in Figure 1e–g, all Ch-NPs including NPs-Ppa, NPs-Cp6, NPs-Ce6, and NPs-Ce4 showed obvious afterglow luminescence with the maximum wavelength centered between 660 and 680 nm, very close to the fluorescence peak positions of the corresponding mother molecules but with different intensities. For example, NPs-Ppa exhibits the strongest fluorescence but the weakest afterglow luminescence. Although NPs-Ce4 show moderate fluorescence intensity, they show the strongest afterglow

luminescence, as quantitatively shown in Figure 1h. These data imply that the chlorin backbone plays a determining role in the generation of near-infrared afterglow luminescence and the substituents on the chlorin backbone can be optimized with respect to the afterglow brightness.

Mechanistic Study of Afterglow. It is worth mentioning that all aforementioned chlorins also showed similar afterglow luminescence in THF (Figure S5), even with the same intensity order as that for the corresponding Ch-NPs in aqueous media, suggesting that the afterglow luminescence is an intrinsic property of the chlorins although the afterglow brightness is largely affected by the substituent on the aromatic ring. It was also observed that Ce4 exhibited afterglow luminescence with different degrees of brightness in different organic solvents such as THF, acetonitrile (ACN), and trichloromethane (CHCl_3). The afterglow intensity of Ce4 in CHCl_3 was 3.0-fold and 8.8-fold that in ACN and THF, respectively, well consistent with the lifetime of $^1\text{O}_2$ in these organic solvents according to literature reports (Figure 2a),^{38–40} indicating that the $^1\text{O}_2$ plays an important role in the afterglow luminescence of chlorins. To verify this hypothesis, a singlet oxygen sensor green (SOSG) was used to detect $^1\text{O}_2$ during the light irradiation process. As shown in Figure 2b, the fluorescence intensity of SOSG at 528 nm was increased by 14.9-fold after irradiation for 5 min, while no obvious fluorescence enhancement was presented by either SOSG or NPs-Ce4 as the control group. Furthermore, the afterglow luminescence of NPs-Ce4 was increased by 1.40-fold after the solution was purged with O_2 but decreased by 1.85-fold when the solution was purged with N_2 or by 1.83-fold when $^1\text{O}_2$ scavenger NaN_3 was introduced (Figure 2c). All of these experiments demonstrate that $^1\text{O}_2$ plays a determining role in the afterglow luminescence of chlorins, which provides opportunities to irradiate the Ch-NPs with different sources. As shown in Figure 2d, the afterglow luminescence from chlorins can also be triggered by an 808 nm laser with the aid of a photosensitizer silicon 2,3-naphthalocyanine bis-(trihexylsilyloxyde) (NCBS), as quantitatively shown in Figure S6. As 808 nm light can penetrate tissues deeper than visible light, the afterglow luminescence of chlorin particles triggered by 808 nm laser significantly broadens the biomedical applications of the current system. In short, the above studies suggest that $^1\text{O}_2$ is necessary for the afterglow luminescence of chlorins irrespective of the way it is generated.

To determine the molecular mechanism for Ce4 to generate the afterglow involving $^1\text{O}_2$, the structural variation of Ce4 was studied after light irradiation. According to the absorption spectra given in Figures 3a and S7, the main absorption of Ce4 peaking at about 400 nm was substantially decreased upon irradiation, indicating that an obvious decomposition of Ce4 occurred, which was accompanied by the generation of a new substance upon exhausted irradiation as indicated by HPLC results shown in Figure 3b. Further, MS analysis indicated that the newly formed substance had a molecular ion peak at $m/z = 333.20$ ($[\text{M} + \text{H}]^+$), and in combination with literature studies, it can be identified as Ce4-F as given in Figure 3c.^{41–44} Therefore, it could be concluded that the conjugated structure of Ce4 was partly broken into tiny fragments along with the afterglow luminescence. As the afterglow could remarkably be retained, e.g., 95.9 and 57.5% room-temperature luminescence intensity was retained when the solution was kept at -20°C for 8 and 24 h, respectively (Figure 3d), it can be deduced that the light energy is stored by an active intermediate species

whose decomposition rate is greatly suppressed at low temperature. The most striking feature of the afterglow of Ch-NPs is the ultralong half-life (Figure 3e), e.g., 1.5 h for NPs-Ce4, 1 order of magnitude higher than those reported for organic semiconducting polymeric afterglow systems,²⁶ suggesting that the active structure generated by chlorins has a much slower decomposition rate, which was also observed from a number of Schaap's adamantlylidene-1,2-dioxetane-based chemiluminescent agents reported in the literature.^{45–50} Based on these results, we propose the following mechanism for the afterglow of chlorins taking Ce4 as an example, i.e., Ce4 passes the absorbed energy to oxygen to produce $^1\text{O}_2$, which subsequently oxidizes the vinylene bond ($\text{C}=\text{C}$) via $[\pi_2 + \pi_2]$ cycloaddition to form a Ce4-dioxetane intermediate, and the decomposition of the Ce4-dioxetane intermediate finally leads to the afterglow luminescence from chlorins. As the afterglow luminescence highly resembles the fluorescence of the corresponding chlorins, it is deduced that the spontaneous decomposition of Ce4-dioxetane transfers proper energy to promote Ce4 to its excited-state Ce4* that is eventually relaxed to its ground state by emitting afterglow luminescence; meanwhile, Ce4-F is generated, as depicted in Figure 3f.

To elucidate the structural impact on the afterglow brightness, the frontier molecular orbitals of the four different chlorins aforementioned were calculated. As shown in Figure 4a,b, the highest occupied molecular orbital (HOMO) levels of

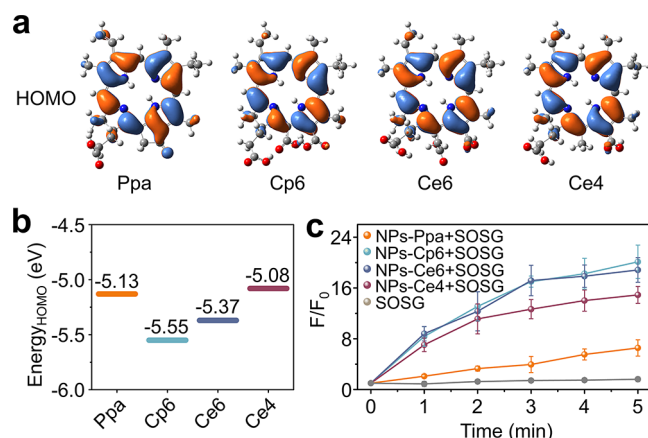


Figure 4. HOMO levels and $^1\text{O}_2$ production capacities of various chlorins. (a, b) HOMO molecular orbitals (a) and HOMO energy levels (b) of chlorins. (c) Concentration of $^1\text{O}_2$ generated by Ch-NPs ($3.5\text{ }\mu\text{M}$), represented by the fluorescence enhancement (F/F_0) of SOSG ($1\text{ }\mu\text{M}$), as a function of irradiation time. The error bars represent standard deviation ($n = 3$).

Ppa, Cp6, Ce6, and Ce4 locate at -5.13 , -5.55 , -5.37 , and -5.08 eV, respectively. Thus, their oxidizability should follow the order of Ce4 > Ppa > Ce6 > Cp6. The high oxidizability is apparently favorable for the formation of the dioxetane intermediate through the reaction between chlorin and $^1\text{O}_2$ and the subsequent afterglow luminescence, which can find supportive evidence from the afterglow brightness order shown in Figure 1e, except for Ppa. In fact, there are two important processes involved in the afterglow luminescence, i.e., the generation of $^1\text{O}_2$ and the dioxetane intermediate. The results given in Figure 4c reveal that Ppa presents the lowest generation rate for $^1\text{O}_2$, while those for Ce4, Ce6, and Cp6 are rather comparable, which well explains the exceptionally

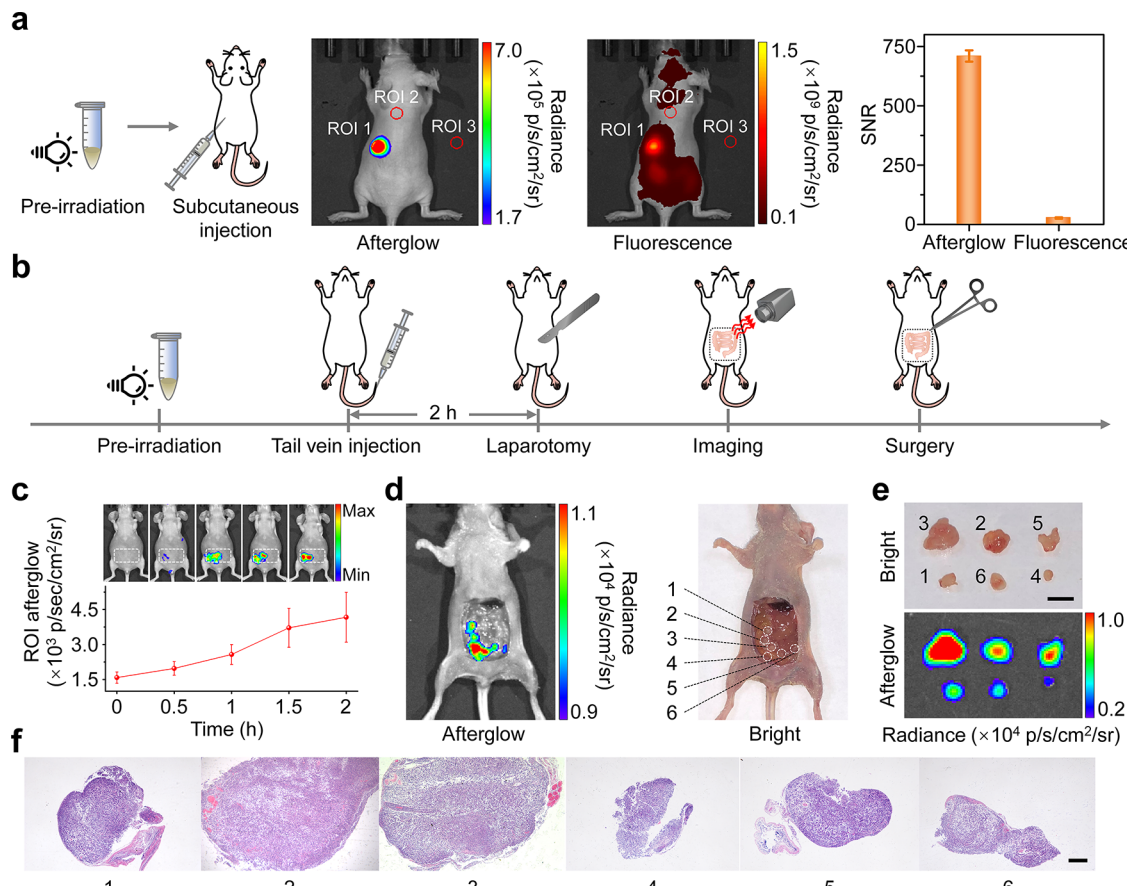


Figure 5. Afterglow imaging of tiny metastatic tumors *in vivo* together with the histological analysis of the tumors extracted. (a) Comparison of afterglow and fluorescence imaging through NPs-Ce4 ($25 \mu\text{g}/\text{mL}, 50 \mu\text{L}$) subcutaneously injected (left) and the quantified SNR was defined as $\text{SNR} = I_{\text{ROI } 1} - I_{\text{ROI } 3}/I_{\text{ROI } 2} - I_{\text{ROI } 3}$ ($n = 3$) (right). (b) Schematic illustrations showing the detailed procedures of the abdominal metastatic tumor detection through the afterglow imaging of NPs-Ce4. (c) Typical afterglow luminescence images recorded at different time points after NPs-Ce4 were intravenously injected into mice, together with the average luminescence intensities of the region of interest (ROI) ($n = 3$). (d) Afterglow and bright-field images of mice that received intravenous injection of NPs-Ce4 ($200 \mu\text{g}/\text{mL}, 200 \mu\text{L}$). (e) Bright-field (top) and afterglow (bottom) images of tumors excised under the guidance of the afterglow signal (the scale bar represents 5 mm). (f) H&E staining images of tumor slices numbered according to those in (e) (the scale bar represents 400 μm).

low afterglow brightness of Ppa although its HOMO level is considerably high among all chlorins.

In Vivo Afterglow Imaging. It was demonstrated that the afterglow luminescence intensity of NPs-Ce4 was linear against the particle concentration, as shown in Figure S8, indicating an ideal capacity of the afterglow for quantitative imaging. As expected, NPs-Ce4 showed no obvious cytotoxicity to cells (Figure S9). In addition, NPs-Ce4 presented a blood elimination half-life of up to approximately 60 min, determined through the fluorescence assays of the blood samples (Figure S10). These advantages encouraged us to carry out animal studies on afterglow imaging of tumors *in vivo*.

To show the advantages of the near-infrared afterglow luminescence over conventional fluorescence with respect to *in vivo* imaging applications, the afterglow and fluorescence images were acquired after subcutaneous injection of NPs-Ce4 into living mice. The SNR of NPs-Ce4 was then determined as depicted in Figure 5a. The quantified results reveal that the SNR of the afterglow is more than 26-fold that of the corresponding fluorescence. The high SNR is conducive to distinguishing tiny tumors that are difficult to identify through fluorescence imaging during clinical surgery, and the ultralong half-life helps save the light reirradiation step, thereby simplifying the imaging process for imaging-guided surgery.

To show these advantages, NPs-Ce4 were used to detect intraperitoneal 4T1 tumors of different sizes in mice. The detailed procedures are given in Figure 5b. It is worth mentioning that NPs-Ce4 were activated only once with light prior to the intravenous injection through the tail vein of mice. The afterglow signal from the abdomen region was then continually monitored through afterglow imaging after the NPs-Ce4 were intravenously injected (Figure 5c). In general, the signal intensity of the region of interest is governed by the natural decay of the afterglow luminescence and the gradually increased accumulation of NPs-Ce4 through the enhanced permeability and retention effect.^{51–53} After careful optimization through the above afterglow imaging studies, laparotomy was performed at 2 h postinjection of NPs-Ce4, followed by afterglow and near-infrared fluorescence imaging to show the possibility of precise tumor resection under the guidance of afterglow luminescence and the advantage of afterglow over conventional fluorescence in this respect. According to the results in Figures 5d and S11, strong afterglow signals were presented by part of the intestines where no identifiable fluorescence signal was observed, and the SNR of the afterglow is more than 18-fold that of the corresponding fluorescence. Under the guidance of the afterglow signal, six pieces of suspicious lesions were resected. The results in Figure 5e reveal

that all of these tissues can still emit afterglow signals after reactivating NPs-Ce4 with light, and the subsequent histological analysis through hematoxylin and eosin (H&E) staining demonstrated that the tissues harvested under the guidance of the afterglow signals are tumorous tissues and the smallest identifiable tumor is 3 mm³ (**Figure 5f**). Apart from the cancerous lesions, the major organs were also extracted and reactivated. The imaging results in **Figure S12** revealed that the lung presented a stronger signal than tumors. However, the lung signal is remarkably shielded by the ribs, muscles, and skin tissues of the chest. In addition, the liver, kidney, gallbladder also exhibited weak afterglow signals. The histological analysis in **Figure S13** revealed that no noticeable changes in the major organs were presented after the intravenous administration of NPs-Ce4, verifying the excellent biocompatibility of the chlorins.

CONCLUSIONS

In this study, we have for the first time demonstrated that chlorins can generate near-infrared afterglow luminescence suitable for the imaging of tiny metastatic tumors *in vivo*. The structural analysis of the product, performed after exhausted irradiation with the same light source used for generating the afterglow luminescence, allowed us to clearly depict the molecular mechanism of the afterglow luminescence, *i.e.*, the chlorin molecule transfers its absorbed photoenergy to oxygen to generate ¹O₂ that subsequently attacks chlorin to form a metastable dioxetane intermediate structure, and the slow decomposition of the dioxetane structure eventually transfers energy to the adjacent chlorin molecules to emit light. Using Ce4 as an example, we have further demonstrated that the near-infrared afterglow, with a half-life of up to 1.5 h, can enable successful resection of metastatic tumors as small as 3 mm³ with a single shot of excitation, which shows well the promising potential of chlorins as afterglow agents. Although the afterglow behavior is an intrinsic nature of chlorins, the above molecular mechanism suggests that the afterglow performance can further be optimized through the substituents on the backbone.

ASSOCIATED CONTENT

Supporting Information

The Supporting Information is available free of charge at <https://pubs.acs.org/doi/10.1021/jacs.1c10168>.

Chemicals; preparative methods; characterizations of chlorins and chlorin nanoparticles; and *in vitro* and *in vivo* experimental details, including Scheme S1 and Figures S1–S13 ([PDF](#))

AUTHOR INFORMATION

Corresponding Authors

Qing Li – State Key Laboratory of Radiation Medicine and Protection, School for Radiological and Interdisciplinary Sciences (RAD-X), Collaborative Innovation Center of Radiation Medicine of Jiangsu Higher Education Institutions, Soochow University, Suzhou 215123, P. R. China;
Email: qli87@suda.edu.cn

Qingqing Miao – State Key Laboratory of Radiation Medicine and Protection, School for Radiological and Interdisciplinary Sciences (RAD-X), Collaborative Innovation Center of Radiation Medicine of Jiangsu Higher Education Institutions, Soochow University, Suzhou 215123, P. R. China;

● orcid.org/0000-0001-8973-6687; Email: qqmiao@suda.edu.cn

Mingyuan Gao – State Key Laboratory of Radiation Medicine and Protection, School for Radiological and Interdisciplinary Sciences (RAD-X), Collaborative Innovation Center of Radiation Medicine of Jiangsu Higher Education Institutions, Soochow University, Suzhou 215123, P. R. China;
● orcid.org/0000-0002-7360-3684; Email: gaomy@iccas.ac.cn

Authors

Wan Chen – State Key Laboratory of Radiation Medicine and Protection, School for Radiological and Interdisciplinary Sciences (RAD-X), Collaborative Innovation Center of Radiation Medicine of Jiangsu Higher Education Institutions, Soochow University, Suzhou 215123, P. R. China

Yuan Zhang – State Key Laboratory of Radiation Medicine and Protection, School for Radiological and Interdisciplinary Sciences (RAD-X), Collaborative Innovation Center of Radiation Medicine of Jiangsu Higher Education Institutions, Soochow University, Suzhou 215123, P. R. China

Yue Jiang – State Key Laboratory of Radiation Medicine and Protection, School for Radiological and Interdisciplinary Sciences (RAD-X), Collaborative Innovation Center of Radiation Medicine of Jiangsu Higher Education Institutions, Soochow University, Suzhou 215123, P. R. China

Hui Zhou – State Key Laboratory of Radiation Medicine and Protection, School for Radiological and Interdisciplinary Sciences (RAD-X), Collaborative Innovation Center of Radiation Medicine of Jiangsu Higher Education Institutions, Soochow University, Suzhou 215123, P. R. China

Yinghua Liu – State Key Laboratory of Radiation Medicine and Protection, School for Radiological and Interdisciplinary Sciences (RAD-X), Collaborative Innovation Center of Radiation Medicine of Jiangsu Higher Education Institutions, Soochow University, Suzhou 215123, P. R. China

Complete contact information is available at:
<https://pubs.acs.org/10.1021/jacs.1c10168>

Notes

The authors declare no competing financial interest.

ACKNOWLEDGMENTS

The authors acknowledge the financial support from the National Key Research and Development Program of China (2018YFA0208800), the National Natural Science Foundation of China (81720108024, 81901803, and 22106115), Jiangsu Specially Appointed Professorship, and Natural Science Foundation of Jiangsu Province (BK20190811 and BK20190830). They are also very grateful for the theoretical calculation guidance by Professor Qiao Sun, State Key Laboratory of Radiation Medicine and Protection, Soochow University.

REFERENCES

- (1) Weissleder, R.; Pittet, M. J. Imaging in the era of molecular oncology. *Nature* **2008**, *452*, 580–589.
- (2) Zhang, R. R.; Schroeder, A. B.; Grudzinski, J. J.; Rosenthal, E. L.; Warram, J. M.; Pinchuk, A. N.; Eliceiri, K. W.; Kuo, J. S.; Weichert, J. P. Beyond the margins: Real-time detection of cancer using targeted fluorophores. *Nat. Rev. Clin. Oncol.* **2017**, *14*, 347–364.
- (3) Urano, Y.; Sakabe, M.; Kosaka, N.; Ogawa, M.; Mitsunaga, M.; Asanuma, D.; Kamiya, M.; Young, M. R.; Nagano, T.; Choyke, P. L.;

- Kobayashi, H. Rapid cancer detection by topically spraying a gamma-glutamyltranspeptidase-activated fluorescent probe. *Sci. Transl. Med.* **2011**, *3*, No. 110ra119.
- (4) Smith, A. M.; Mancini, M. C.; Nie, S. Bioimaging: Second window for *in vivo* imaging. *Nat. Nanotechnol.* **2009**, *4*, 710–711.
- (5) Miao, Q.; Pu, K. Organic semiconducting agents for deep-tissue molecular imaging: Second near-infrared fluorescence, self-luminescence, and photoacoustics. *Adv. Mater.* **2018**, *30*, No. 1801778.
- (6) Li, Q.; Zeng, J.; Miao, Q.; Gao, M. Self-illuminating agents for deep-tissue optical imaging. *Front. Bioeng. Biotechnol.* **2019**, *7*, No. 326.
- (7) Hai, Z.; Li, J.; Wu, J.; Xu, J.; Liang, G. Alkaline phosphatase-triggered simultaneous hydrogelation and chemiluminescence. *J. Am. Chem. Soc.* **2017**, *139*, 1041–1044.
- (8) Chen, Y.; Wu, C.; Wang, C.; Zhang, T.; Hua, Y.; Shen, Y.; Liang, G. Bioluminescence imaging of urokinase-type plasminogen activator activity *in vitro* and in tumors. *Anal. Chem.* **2021**, *93*, 9970–9973.
- (9) Lu, L.; Li, B.; Ding, S.; Fan, Y.; Wang, S.; Sun, C.; Zhao, M.; Zhao, C. X.; Zhang, F. NIR-II bioluminescence for *in vivo* high contrast imaging and *in situ* ATP-mediated metastases tracing. *Nat. Commun.* **2020**, *11*, No. 4192.
- (10) Yang, Y.; Wang, S.; Lu, L.; Zhang, Q.; Yu, P.; Fan, Y.; Zhang, F. NIR-II chemiluminescence molecular sensor for *in vivo* high-contrast inflammation imaging. *Angew. Chem., Int. Ed.* **2020**, *59*, 18380–18385.
- (11) Jiang, Y.; Pu, K. Molecular probes for autofluorescence-free optical imaging. *Chem. Rev.* **2021**, *121*, 13086–13131.
- (12) Green, O.; Gnaim, S.; Blau, R.; Eldar-Boock, A.; Satchi-Fainaro, R.; Shabat, D. Near-infrared dioxetane luminophores with direct chemiluminescence emission mode. *J. Am. Chem. Soc.* **2017**, *139*, 13243–13248.
- (13) Van de Bittner, G. C.; Bertozzi, C. R.; Chang, C. J. Strategy for dual-analyte luciferin imaging: *In vivo* bioluminescence detection of hydrogen peroxide and caspase activity in a murine model of acute inflammation. *J. Am. Chem. Soc.* **2013**, *135*, 1783–1795.
- (14) Badr, C. E.; Tannous, B. A. Bioluminescence imaging: Progress and applications. *Trends Biotechnol.* **2011**, *29*, 624–633.
- (15) Suzuki, K.; Nagai, T. Recent progress in expanding the chemiluminescent toolbox for bioimaging. *Curr. Opin. Biotechnol.* **2017**, *48*, 135–141.
- (16) Xu, S.; Chen, R.; Zheng, C.; Huang, W. Excited state modulation for organic afterglow: Materials and applications. *Adv. Mater.* **2016**, *28*, 9920–9940.
- (17) Palner, M.; Pu, K.; Shao, S.; Rao, J. Semiconducting polymer nanoparticles with persistent near-infrared luminescence for *in vivo* optical imaging. *Angew. Chem., Int. Ed.* **2015**, *54*, 11477–11480.
- (18) Abdukayum, A.; Chen, J. T.; Zhao, Q.; Yan, X. P. Functional near infrared-emitting Cr³⁺/Pr³⁺ co-doped zinc gallogermanate persistent luminescent nanoparticles with superlong afterglow for *in vivo* targeted bioimaging. *J. Am. Chem. Soc.* **2013**, *135*, 14125–14133.
- (19) Fan, W.; Lu, N.; Xu, C.; Liu, Y.; Lin, J.; Wang, S.; Shen, Z.; Yang, Z.; Qu, J.; Wang, T.; Chen, S.; Huang, P.; Chen, X. Enhanced afterglow performance of persistent luminescence implants for efficient repeatable photodynamic therapy. *ACS Nano* **2017**, *11*, 5864–5872.
- (20) Cui, D.; Xie, C.; Li, J.; Lyu, Y.; Pu, K. Semiconducting photosensitizer-incorporated copolymers as near-infrared afterglow nanoagents for tumor imaging. *Adv. Healthcare Mater.* **2018**, *7*, No. 1800329.
- (21) Wang, J.; Li, J.; Yu, J.; Zhang, H.; Zhang, B. Large hollow cavity luminous nanoparticles with near-infrared persistent luminescence and tunable sizes for tumor afterglow imaging and chemo-/photodynamic therapies. *ACS Nano* **2018**, *12*, 4246–4258.
- (22) Xie, C.; Zhen, X.; Miao, Q.; Lyu, Y.; Pu, K. Self-assembled semiconducting polymer nanoparticles for ultrasensitive near-infrared afterglow imaging of metastatic tumors. *Adv. Mater.* **2018**, *30*, No. 1801331.
- (23) Jiang, Y.; Huang, J.; Zhen, X.; Zeng, Z.; Li, J.; Xie, C.; Miao, Q.; Chen, J.; Chen, P.; Pu, K. A generic approach towards afterglow luminescent nanoparticles for ultrasensitive *in vivo* imaging. *Nat. Commun.* **2019**, *10*, No. 2064.
- (24) Wu, L.; Ishigaki, Y.; Hu, Y.; Sugimoto, K.; Zeng, W.; Harimoto, T.; Sun, Y.; He, J.; Suzuki, T.; Jiang, X.; Chen, H. Y.; Ye, D. H₂S-activatable near-infrared afterglow luminescent probes for sensitive molecular imaging *in vivo*. *Nat. Commun.* **2020**, *11*, No. 446.
- (25) Xu, Y.; Yang, W.; Yao, D.; Bian, K.; Zeng, W.; Liu, K.; Wang, D.; Zhang, B. An aggregation-induced emission dye-powered afterglow luminogen for tumor imaging. *Chem. Sci.* **2020**, *11*, 419–428.
- (26) Miao, Q.; Xie, C.; Zhen, X.; Lyu, Y.; Duan, H.; Liu, X.; Jokerst, J. V.; Pu, K. Molecular afterglow imaging with bright, biodegradable polymer nanoparticles. *Nat. Biotechnol.* **2017**, *35*, 1102–1110.
- (27) He, S.; Xie, C.; Jiang, Y.; Pu, K. An organic afterglow protheranostic nanoassembly. *Adv. Mater.* **2019**, *31*, No. 1902672.
- (28) Lyu, Y.; Cui, D.; Huang, J.; Fan, W.; Miao, Y.; Pu, K. Near-infrared afterglow semiconducting nano-polycomplexes for the multiplex differentiation of cancer exosomes. *Angew. Chem., Int. Ed.* **2019**, *58*, 4983–4987.
- (29) Pei, P.; Chen, Y.; Sun, C.; Fan, Y.; Yang, Y.; Liu, X.; Lu, L.; Zhao, M.; Zhang, H.; Zhao, D.; Liu, X.; Zhang, F. X-ray-activated persistent luminescence nanomaterials for NIR-II imaging. *Nat. Nanotechnol.* **2021**, *16*, 1011–1018.
- (30) Wang, Y.; Song, G.; Liao, S.; Qin, Q.; Zhao, Y.; Shi, L.; Guan, K.; Gong, X.; Wang, P.; Yin, X.; Chen, Q.; Zhang, X. B. Cyclic amplification of the afterglow luminescent nanoreporter enables the prediction of anti-cancer efficiency. *Angew. Chem., Int. Ed.* **2021**, *60*, 19779–19789.
- (31) Zhen, X.; Xie, C.; Pu, K. Temperature-correlated afterglow of a semiconducting polymer nanococktail for imaging-guided photothermal therapy. *Angew. Chem., Int. Ed.* **2018**, *57*, 3938–3942.
- (32) Ni, X.; Zhang, X.; Duan, X.; Zheng, H. L.; Xue, X. S.; Ding, D. Near-infrared afterglow luminescent aggregation-induced emission dots with ultrahigh tumor-to-liver signal ratio for promoted image-guided cancer surgery. *Nano Lett.* **2019**, *19*, 318–330.
- (33) Zheng, X.; Wu, W.; Zheng, Y.; Ding, Y.; Xiang, Y.; Liu, B.; Tong, A. Organic nanoparticles with persistent luminescence for *in vivo* afterglow imaging-guided photodynamic therapy. *Chem. - Eur. J.* **2021**, *27*, 6911–6916.
- (34) Ramirez-Garcia, G.; Gutierrez-Granados, S.; Gallegos-Corona, M. A.; Palma-Tirado, L.; d'Orlye, F.; Varenne, A.; Mignet, N.; Richard, C.; Martinez-Alfaro, M. Long-term toxicological effects of persistent luminescence nanoparticles after intravenous injection in mice. *Int. J. Pharm.* **2017**, *532*, 686–695.
- (35) Li, Y.; Gecevicius, M.; Qiu, J. Long persistent phosphors—from fundamentals to applications. *Chem. Soc. Rev.* **2016**, *45*, 2090–2136.
- (36) Li, X. Z.; Yin, C.; Liew, S. S.; Lee, C. S.; Pu, K. Y. Organic semiconducting luminophores for near-infrared afterglow, chemiluminescence, and bioluminescence imaging. *Adv. Funct. Mater.* **2021**, *31*, No. 2106154.
- (37) Meng, Z.; Yu, B.; Han, G.; Liu, M.; Shan, B.; Dong, G.; Miao, Z.; Jia, N.; Tan, Z.; Li, B.; Zhang, W.; Zhu, H.; Sheng, C.; Yao, J. Chlorin p6-based water-soluble amino acid derivatives as potent photosensitizers for photodynamic therapy. *J. Med. Chem.* **2016**, *59*, 4999–5010.
- (38) Hurst, J. R.; McDonald, J. D.; Schuster, G. B. Lifetime of singlet oxygen in solution directly determined by laser spectroscopy. *J. Am. Chem. Soc.* **1982**, *104*, 2065–2067.
- (39) Schweitzer, C.; Schmidt, R. Physical mechanisms of generation and deactivation of singlet oxygen. *Chem. Rev.* **2003**, *103*, 1685–1757.
- (40) Thorning, F.; Jensen, F.; Ogilby, P. R. Modeling the effect of solvents on nonradiative singlet oxygen deactivation: Going beyond weak coupling in intermolecular electronic-to-vibrational energy transfer. *J. Phys. Chem. B* **2020**, *124*, 2245–2254.
- (41) Bonnett, R.; Martinez, G. Photobleaching of sensitizers used in photodynamic therapy. *Tetrahedron* **2001**, *57*, 9513–9547.
- (42) Vacher, M.; Galvan, I. F.; Ding, B. W.; Schramm, S.; Berraudo-Pache, R.; Naumov, P.; Ferre, N.; Liu, Y. J.; Navizet, I.; Roca-Sanjuan,

D.; Baader, W. J.; Lindh, R. Chemi- and bioluminescence of cyclic peroxides. *Chem. Rev.* **2018**, *118*, 6927–6974.

(43) Zhao, Z.; Zhang, M. W.; Hurren, C.; Zhou, L. M.; Wu, J. H.; Sun, L. Study on photofading of two natural dyes sodium copper chlorophyllin and gardenia yellow on cotton. *Cellulose* **2020**, *27*, 8405–8427.

(44) Luo, T.; Ni, K.; Culbert, A.; Lan, G.; Li, Z.; Jiang, X.; Kaufmann, M.; Lin, W. Nanoscale metal-organic frameworks stabilize bacteriochlorins for type I and type II photodynamic therapy. *J. Am. Chem. Soc.* **2020**, *142*, 7334–7339.

(45) Hananya, N.; Press, O.; Das, A.; Scomparin, A.; Satchi-Fainaro, R.; Sagi, I.; Shabat, D. Persistent chemiluminescent glow of phenoxy-dioxetane luminophore enables unique CRET-based detection of proteases. *Chemistry* **2019**, *25*, 14679–14687.

(46) Hananya, N.; Shabat, D. Recent advances and challenges in luminescent imaging: Bright outlook for chemiluminescence of dioxetanes in water. *ACS Cent. Sci.* **2019**, *5*, 949–959.

(47) Son, S.; Won, M.; Green, O.; Hananya, N.; Sharma, A.; Jeon, Y.; Kwak, J. H.; Sessler, J. L.; Shabat, D.; Kim, J. S. Chemiluminescent probe for the *in vitro* and *in vivo* imaging of cancers over-expressing NQO1. *Angew. Chem., Int. Ed.* **2019**, *58*, 1739–1743.

(48) An, R.; Wei, S.; Huang, Z.; Liu, F.; Ye, D. An activatable chemiluminescent probe for sensitive detection of gamma-glutamyl transpeptidase activity *in vivo*. *Anal. Chem.* **2019**, *91*, 13639–13646.

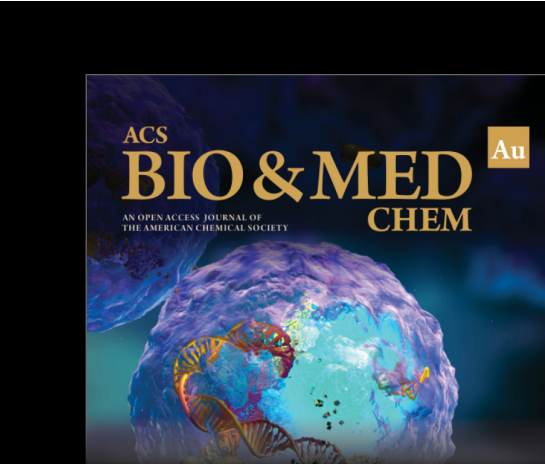
(49) Roth-Konforti, M.; Green, O.; Hupfeld, M.; Fieseler, L.; Heinrich, N.; Ihssen, J.; Vorberg, R.; Wick, L.; Spitz, U.; Shabat, D. Ultrasensitive detection of *Salmonella* and *Listeria monocytogenes* by small-molecule chemiluminescence probes. *Angew. Chem., Int. Ed.* **2019**, *58*, 10361–10367.

(50) Shelef, O.; Sedgwick, A. C.; Pozzi, S.; Green, O.; Satchi-Fainaro, R.; Shabat, D.; Sessler, J. L. Turn on chemiluminescence-based probes for monitoring tyrosinase activity in conjunction with biological thiols. *Chem. Commun.* **2021**, *57*, 11386–11389.

(51) Greish, K. Enhanced permeability and retention (EPR) effect for anticancer nanomedicine drug targeting. *Methods Mol. Biol.* **2010**, *624*, 25–37.

(52) Petros, R. A.; DeSimone, J. M. Strategies in the design of nanoparticles for therapeutic applications. *Nat. Rev. Drug Discov.* **2010**, *9*, 615–627.

(53) Zeng, J.; Jing, L.; Hou, Y.; Jiao, M.; Qiao, R.; Jia, Q.; Liu, C.; Fang, F.; Lei, H.; Gao, M. Anchoring group effects of surface ligands on magnetic properties of Fe₃O₄ nanoparticles: Towards high performance MRI contrast agents. *Adv. Mater.* **2014**, *26*, 2694–2698.



Editor-in-Chief: Prof. Shelley D. Minteer, University of Utah, USA

Deputy Editor
Prof. Squire J. Booker
Pennsylvania State University, USA

Open for Submissions 

pubs.acs.org/biomedchemau  ACS Publications
Most Trusted. Most Cited. Most Read.